

# Fast Muon Tracking with Machine Learning Implemented in FPGA

Chang Sun<sup>a</sup>, Takumi Nakajima<sup>a,\*</sup>, Yuki Mitsumori<sup>a</sup>, Yasuyuki Horii<sup>a,\*\*</sup>, Makoto Tomoto<sup>a,b</sup>

<sup>a</sup>*Nagoya University, Chikusa-ku, Nagoya 464-8602, Japan*

<sup>b</sup>*High Energy Accelerator Research Organisation (KEK), Oho, Tsukuba 305-0801, Japan*

## Abstract

In this work, we present a new approach for fast tracking on multiwire proportional chambers with neural networks. The tracking networks are developed and adapted for the first-level trigger at hadron collider experiments. We use Monte Carlo samples generated by Geant4 with a custom muon chamber, which resembles part of the thin gap chambers from the ATLAS experiment, for training and performance evaluations. The chamber has a total of seven gas gaps, where the first and last gas gaps are displaced by  $\sim 1.5$  m. Each gas gap has 50 channels with a size of 18–20 mm. Two neural network models are developed and presented: a convolutional neural network and a neural network optimized for the detector configuration of this study. In the latter network, a convolution layer is provided for each of three groups formed from 2–3 gas gaps of the chamber, and the outputs are fed into multilayer perceptrons in sequence. Both networks are transformed into hardware description language and implemented in Virtex UltraScale+ FPGA. The angular resolution is 2 mrad, which is comparable to the maximum resolution of the detector estimated by the minimum  $\chi^2$  method. The latency achieved by the implemented firmware is less than 100 ns, and the throughput rate is 160 MHz.

**Keywords:** Muon Tracking, Machine Learning, Field-Programmable Gate Array, Artificial Neural Network

## 1. Introduction

Triggering muons is critically important in proton-proton collider experiments. For instance, in 2012, a new particle with a mass of approximately 125 GeV was observed at the ATLAS and CMS experiments [1, 2] using a muon trigger [3, 4] at the CERN Large Hadron Collider (LHC). Subsequent measurements indicate that the new particle is consistent with the Higgs boson in the standard model [5, 6].

An upgrade to the LHC, which is known as the High-Luminosity LHC (HL-LHC), is expected to become operational in 2027 [7]. The peak luminosity of the HL-LHC would ultimately be increased to  $7.5 \times 10^{34} \text{ cm}^{-2}\text{s}^{-1}$ , which is 7.5 times the design luminosity of the LHC ( $1 \times 10^{34} \text{ cm}^{-2}\text{s}^{-1}$ ). The trigger and data-acquisition system of the ATLAS experiment requires upgrades [8] to accommodate the increase in luminosity. In the original first-level muon trigger, only selected and processed hit data of the muon spectrometer are transferred from the front-end to the backend electronics. However, the new system will send all hit data to the backend electronics, exploiting advances in data-transfer technology, and all hits will be processed using high-end FPGAs integrated into the backend electronics.

The ability of backend FPGAs to retrieve full hit data provides a unique opportunity to boost the first-level muon trigger's performance. A throughput of  $\geq 40$  MHz and a latency within  $\mathcal{O}(100 \text{ ns})$  are required. One method proposed for the new system is a fast tracking algorithm known as “pattern matching” [8], which compares the received hit data with predefined hit lists with corresponding track information assigned. Another possibility, which is the subject of this paper, is to use a neural network to perform fast tracking, exploiting the augmented on-board computing power. Here, the hit data are used as the neural network's input, and the track information is outputted.

Machine learning techniques are rapidly being developed for and applied in high-energy physics experiments. A living review is provided in Ref. [9]. Refs. [10, 11, 12, 13] show how different architectures can be deployed on a first-level trigger using the hls4ml library. These works have opened a new era for using machine learning for trigger systems. Novel fast tracking on a silicon detector has been and continues to be developed [8, 14, 15, 16]; however, the use of machine learning is challenging because of the large number of channels. A muon chamber has fewer channels, and fast muon tracking with machine learning has been attempted [17].

In this study, a novel approach of using neural networks for online muon tracking is introduced. Neural network models are developed for the first-level muon trigger at high-luminosity hadron colliders. Two neural network models are implemented in Xilinx Virtex UltraScale+ FPGA and are tested on Monte Carlo (MC) samples through Vi-

\*Co-first author

\*\*Corresponding author

Email address: yhorii@hepl.phys.nagoya-u.ac.jp (Yasuyuki Horii)

vado post-implementation simulations [18]. The tracking performance, latency, and required FPGA resources are evaluated with different hyper parameters. For the tracking performance, focus is placed on the angular resolution, which is critical for the momentum determination (and hence the trigger rate) at the first-level muon trigger [8]. The dependence of the tracking performance on the detector noise level is also studied.

The remainder of this paper is organized as follows. The model for the MC sample as well as the tracking performance by a conventional minimum  $\chi^2$  method is described in Section 2. The workflow and software are introduced in Section 3. The network design and evaluations for the two types of networks are described in Sections 4 and 5. The conclusion is provided in Section 6.

## 2. Simulation

### 2.1. Simulation samples

The networks presented in this work were trained and evaluated on events simulated with Geant4 [19]. In the simulation, a gas chamber detector shape similar to the thin gap chamber (TGC) of the ATLAS experiment [20] was formed with an approximate pseudorapidity ( $\eta$ ) coverage of  $2.03 \leq |\eta| \leq 2.26$ . A full schematic of the detector model used is shown in Fig. 1. Rectangular plates were used instead of the trapezoidal plates of the TGC detector for simplicity. The angular resolution of the tracking shown in this paper is independent from the simplifications of the detector geometry because the wire orientations are identical. Three plates—one triplet and two doublet plates—were used in the simulation. The triplet plate corresponds to the TGC’s innermost plate and has dimensions of  $900 \text{ mm} \times 500 \text{ mm} \times 70 \text{ mm}$ . The two doublet plates correspond to the TGC’s outer plates and have dimensions of  $990 \text{ mm} \times 500 \text{ mm} \times 44 \text{ mm}$ . The triplet plate is named M1, and the doublet plates are named M2 and M3. All the plates were positioned with their central points set to the TGC plates’ central positions. The  $z$  positions<sup>1</sup> of the M1, M2, and M3 plates were identical to TGC’s plates (Fig. 2). The wire pitch for all the plates was 1.8 mm, and 10 (11) wires were grouped into channels for triplet (doublet) plates. No magnetic field was introduced because the TGC detector is located outside the toroidal magnet at the ATLAS experiment.

The muon source was placed in front of the M1 plate at  $z = 13.3 \text{ m}$ . Multiple scattering and emissions before arriving at the muon chamber were ignored because the intrinsic performance of the tracking with the muon chamber was the topic of interest. At the ATLAS experiment, muons with transverse momentum  $p_T \geq 20 \text{ GeV}$  are deflected, at most,  $\pm 30 \text{ mrad}$  from the trajectory of muons

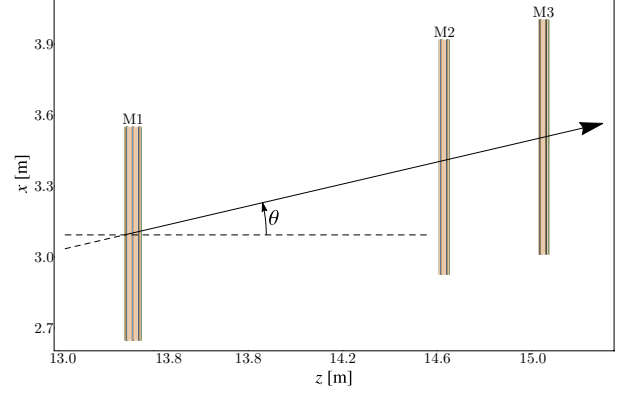


Figure 1: Schematic of the detector model. The  $z$  coordinates of the chambers are identical to those of TGC detectors in the ATLAS experiment. The three plates—M1, M2, and M3 in ascending  $z$ -position order—are aligned with their normals parallel to the  $z$  axis. The arrow represents an incoming muon, and  $\theta$  is defined as the polar angle.

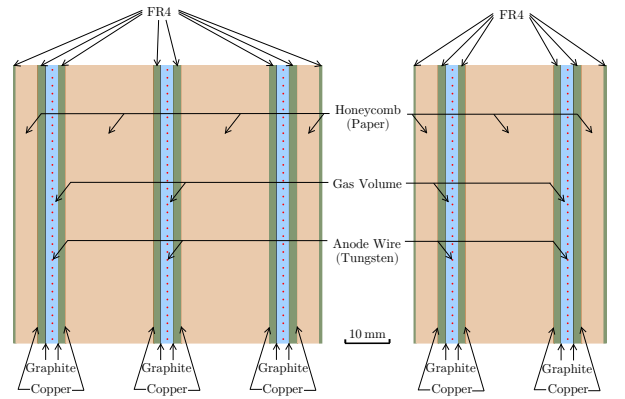


Figure 2: Cross-sectional view of the triplet (left) and doublet (right) plates.

<sup>1</sup>The  $z$  axis is taken as the proton beam axis in the ATLAS experiment, and is taken accordingly in this study.

with infinite momentum when impacting the TGC detector. The sign of the deflection angle depends on the electric charge of the muon. In this study, muons' direction was uniformly distributed in the range  $\pm 30$  mrad from the angle of the straight track, which was independently uniformly distributed on the polar angle  $\theta$ . The straight tracks were aligned directly from the interaction point. A single muon was generated for each event. Tracking of the minimum ionizing particle is critical for muon triggering at the ATLAS experiment, and all muons were generated with  $p_T = 20$  GeV in this study. All data associated with tracks passing through all seven gas gaps were collected for both training and performance evaluation. A channel generated a readout value of 1 if it was fired and 0 if not. The fired channels are referred to as “hits” in this work.

With the aforementioned settings,  $3 \times 10^6$  events were generated for this study. Twenty percent of the data was used as the test set, which was not exposed to any models introduced in this study prior to the performance analysis.

To achieve a more realistic background environment, we prepared extra simulation samples with artificial noises. These samples are generated by randomly setting the readout value to 1 with probability  $p$  for all channels independently of the generated dataset. Hereafter,  $p$  is represented as the “noise level”.

The channel-wise correlation matrices of the channel outputs between the plates are shown in Fig. 3. The elements of the correlation matrices, the correlation coefficients  $\rho_{i,j}$ , are defined as  $\rho_{i,j} \equiv E[\{x_i - E(x_i)\}\{x_j - E(x_j)\}] / \sqrt{E[\{x_i - E(x_i)\}^2]E[\{x_j - E(x_j)\}^2]}$ , where  $x$  is 1 if the corresponding channel has a hit and 0 otherwise,  $i$  and  $j$  are the channel identifiers for the given two plates, and  $E$  represents the expectation value. These correlation matrices were used for determining some of the hyper parameters and for reducing the number of multiplication operations required by the network.

## 2.2. Reference tracking performance

For reference, the best possible resolution of this detector was estimated using the minimum  $\chi^2$  method. In each event, one straight line was randomly placed in the detector's volume according to the distribution of muon trajectories, as described in Section 2.1, and all channels passed by the line were marked as fired. Because there was no false hit, an ordinary  $\chi^2$  fit was used to estimate the resolution. Specifically, when a gas gap had exactly one hit, the coordinate of the center of the channel was used for the fit with an error  $\sigma$ ; if a gas gap had two adjacent hits, the coordinate of the center of the two channels combined with an error  $\sigma/\sqrt{2}$  was used for the fit. This method is referred to as “ideal  $\chi^2$ ” in this work. The detector's angular resolution determined by this method is 1.7 mrad.

The performance determined from a  $\chi^2$ -fitting method iterating through all viable hit combinations was evaluated for comparison to the network in this study on the

simulated events. The exact algorithm used for this fit is described as follows: 1) One hit was taken from each gas gap with non-zero hits, and a simple  $\chi^2$  fit was performed for all combinations. 2) The fitted track with the lowest  $\chi^2$  score was selected as the output. Here, given the uniform channel sizes, the hits from the same plate were regarded as having the same uncertainty. This method is referred to as “iterative  $\chi^2$ ” in this work. The angular resolution obtained in this manner for the simulated events is 2.2 mrad. Although the iterative  $\chi^2$  method is more resistant to noises, it uses a maximum of one hit per gas gap and does not fully exploit the position information for a muon that provides hits in two neighboring channels.

## 3. Workflow

All neural networks used in this study were first defined and trained using Keras 2.4.3 [21] and QKeras 0.8.0 [13] with TensorFlow 2.2.0 [22] as the backend. The networks were then translated into an intermediate C++ script using hls4ml 0.5.0 [10] with the setup of `ReuseFactor = 1`, `Strategy = Latency`, and `IOType = io_parallel`. The synthesis was performed with Vivado HLS 2020.1 [23]. The implementation was carried out with Vivado 2020.1 [18], targeting a Xilinx Virtex UltraScale+ XCVU13P FPGA<sup>2</sup> with a clock frequency of 160 MHz. The performance was evaluated with a post-implementation functional simulation running on the Vivado software.

## 4. Muon tracking with convolutional neural networks

### 4.1. Network design

A convolutional neural network (CNN) is a class of deep neural network, widely applied to the analyses of visual images. In this study, the detector outputs were considered to be visual images and muon tracks were reconstructed by a CNN. The input of the network was the hit information for all channels ( $50 \times 7$ ) and the output was the muon track angle  $\theta$ .

A large-scale network that maximizes the muon tracking performance was designed; its schematic is shown in Fig. 4(a). This design was primarily inspired by the VGG network [24]. Multiple convolution layers extract the features of the muon track, and the affine (also known as fully connected) layers located after the convolution layers extract the muon track angle from the extracted features. This network is denoted as software (**SW**).

A compact version of the network was designed by downscaling the **SW** network with the objective of reducing FPGA resource utilization and achieving a smaller latency value. This network is referred to as baseline (**BL**), and its schematic is shown in Fig. 4(b).

<sup>2</sup>XCVU13P-L2FHGA2104E

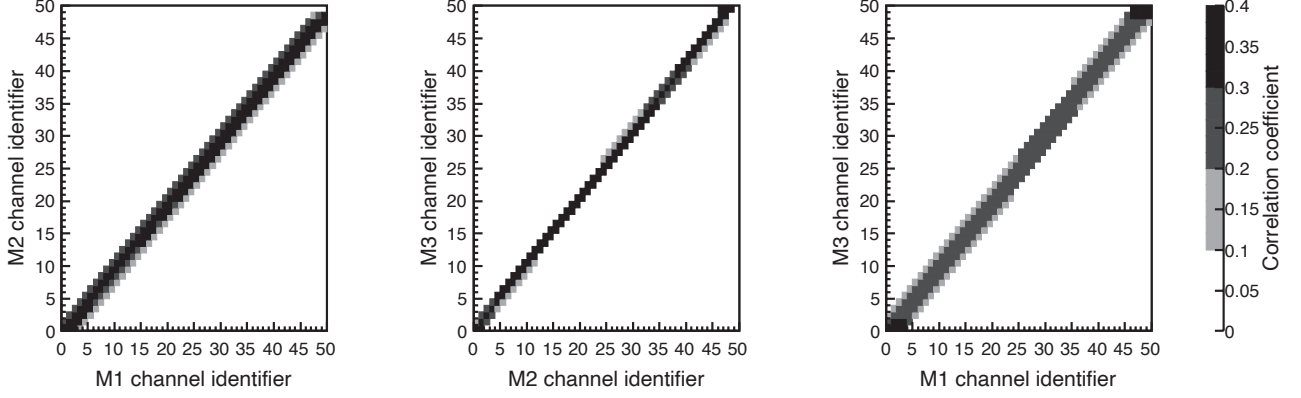


Figure 3: Channel-wise correlation matrices for combinations of the M1, M2, and M3 plates.

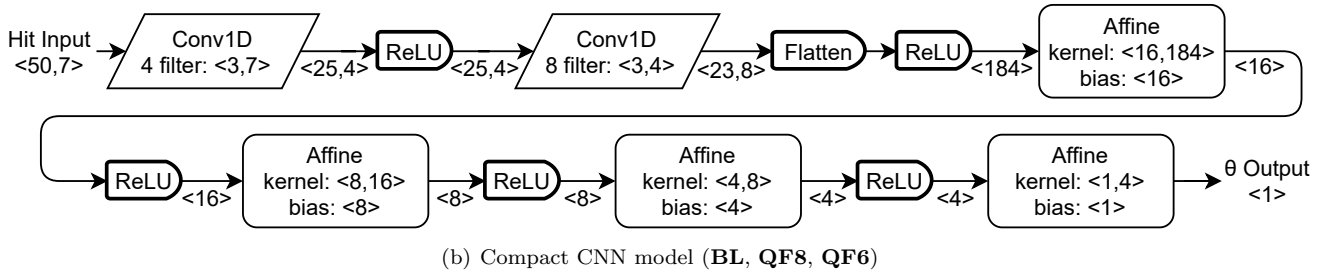
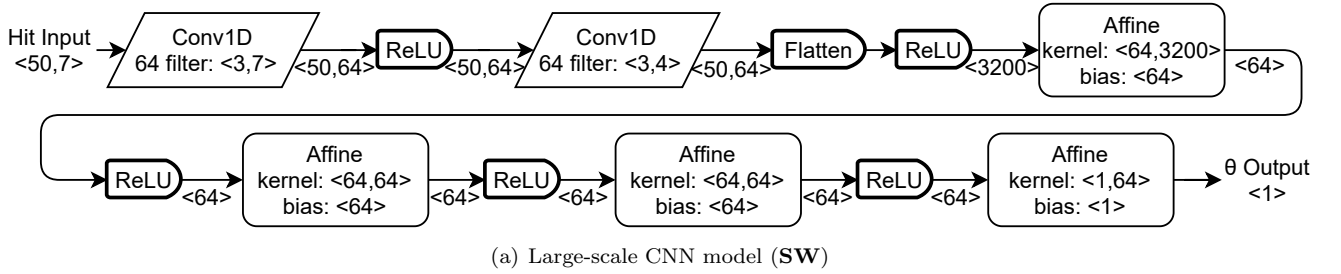


Figure 4: Schematics of the large-scale and compact CNN models. Both are composed of two convolution (“Conv1D”) layers and four affine (“Affine”) layers. The kernel size for the Affine layers refers to  $\langle \text{output dimension}, \text{input dimension} \rangle$ . The kernel size for Conv1D layers refers to filter size and  $\langle \text{input channel}, \text{filter count} \rangle$ . The  $\langle * \rangle$  notation on arrows indicates that the array shape passed through the arrow.

The filter sizes of convolution layers were chosen to cover almost all hits from a single muon track. The exact numbers were determined by the channel-wise correlation matrix shown in Fig. 3.

Quantization was performed on the compact network to further reduce FPGA resource utilization and latency. All parameters, including weights, biases, and intermediate values, in the quantized networks were quantized to `ap_fixed<.,.>` or `ap_ufixed<.,.>`. Overflow and round behaviors were set to be default with wraparound (`AP_WRAP`) and truncation to minus infinity (`AP_TRN`). The numbers of integer bits assigned to each layer’s weights, biases, and intermediate values were selected to be the minimum number such that no overflow would occur for the entire training set. By contrast, the number of float bits assigned ( $n$ ) was fixed for all parameters except accumulators, which had  $(n + 2)$  float bits instead of  $n$ . As the only exception to this rule, the output layer always had 9 unsigned integer bits and 7 float bits. A network quantized with  $n$  float bits assigned is denoted as **QF**[ $n$ ]. Here,  $n = 8$  and 6 were used for the compact network, and the resultant quantized compact networks are referred to as **QF8** and **QF6**, respectively. Because no significant performance difference was observed between post-training quantization and quantization-aware training, only post-training quantization was performed.

All the networks were fully pipelined and able to accept an event every  $1/(160 \text{ MHz}) = 6.25 \text{ ns}$ . No initialization was required between the processing of consecutive events, which is a key feature of the designed network to be used at the first-level trigger at hadron-collider experiments.

#### 4.2. Performance

The angular resolution was evaluated from the widths of the distributions of the difference between the CNN output and the MC truth angle. Figure 5 shows the distributions for the **QF8** network. The distributions of the ideal and iterative  $\chi^2$  methods are also shown for reference. Table 1 shows the values of the angular resolution for the networks examined in this study. The **SW** network provides the best angular resolution of 1.7 mrad. The angular resolution of the **BL**, **QF8**, and **QF6** networks ranges from 2.0 to 3.4 mrad.

The latency and the resource utilization were obtained for the quantized networks and are summarized in Table 1. Both the **QF8** and **QF6** networks were implemented on Vivado without timing violation and achieved a latency less than 100 ns.

### 5. Muon tracking with multistage neural networks

#### 5.1. Network design

We designed another network to take maximum advantage of the strong correlation of the hits between plates of the detector. A schematic of the network is shown in Fig. 6. The hit information on the channels from plates

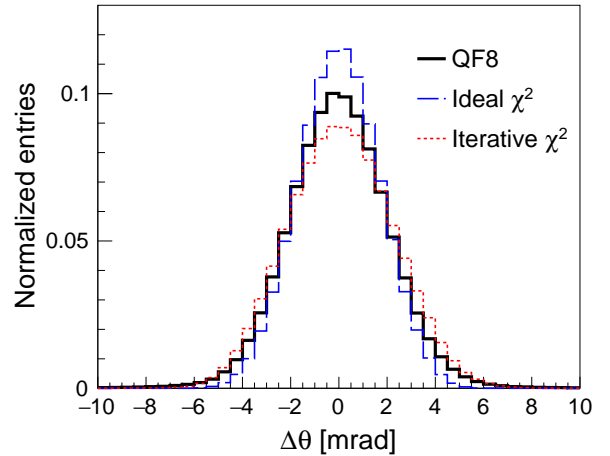


Figure 5: Distributions of the angle difference between the MC truth track segment and the reconstructed track segment. The solid (black) histogram shows the distribution for the track segments reconstructed by the **QF8** network. The dashed (blue) and dotted (red) histograms show the distributions for track segments reconstructed by the ideal and iterative  $\chi^2$  methods, respectively.

M1, M2, and M3 were fed into the network separately in the form of 1-bit arrays of shapes  $\langle 50 \times 3 \rangle$ ,  $\langle 50 \times 2 \rangle$ , and  $\langle 50 \times 2 \rangle$ , respectively. The network consists of two building blocks: a feature-extraction network that exploits the layered structure of the detectors and a generic fully-connected net that outputs the final values.

The design of the feature extraction part was inspired by the track-following scheme [25], where multiple hits are combined together by detector stations and added sequentially in the inside-out direction to form the full track. The convolution layers extract real vectors encoding hit-position information from each plate, whereas the “masked linear” layers (i.e., highly sparse affine layers) define search windows and project the track information from one plate to the next as real vectors. The previous track information (i.e., the output of the last masked linear layer) is merged with the current observation (i.e., the output of the convolution layer) via a simple addition followed by a hyperbolic tangent activation function to allow some inefficiency for the detector while still favoring the track with more hits.

Channel-wise correlation matrices between the plates (Fig. 3) were used to reduce the number of multiplication operations required by the networks. We defined the search windows encoded in the masked linear layers by requiring a correlation coefficient greater than 0.01. All weights outside the windows were constrained to be zero. This practice was responsible for the highly sparse nature of the masked linear layers, where the sparsity was  $\sim 90\%$ . A graphical explanation of how the masked linear layers work is provided in Fig. 7.

The network with full precision in the software simulation is referred to as the **BL** network. Three quantized networks were built from the **BL** network following the procedure specified in Section 4, except that, after quan-

Table 1: The angular resolution, latency, and resource utilization for CNN examined in this study. The numbers in parentheses show the rates of the resource utilization per super logic region. The angular resolutions for **SW** and **BL** are estimated using software, whereas those for **QF8** and **QF6** are estimated using a Vivado post-implementation simulation. The **SW** and **BL** networks are provided without the intention to be run on the hardware; thus, the values of the latency and resource utilization are omitted.

Model	Resolution [mrad]	Latency [ns]	DSP48	LUT	FF	BRAM
<b>SW</b>	1.7	-	-	-	-	-
<b>BL</b>	2.0	-	-	-	-	-
<b>QF8</b>	2.2	81	2087 (68%)	66,441 (15%)	19,849 (2%)	0 (0%)
<b>QF6</b>	3.4	81	607 (20%)	61,749 (14%)	11,702 (1%)	0 (0%)

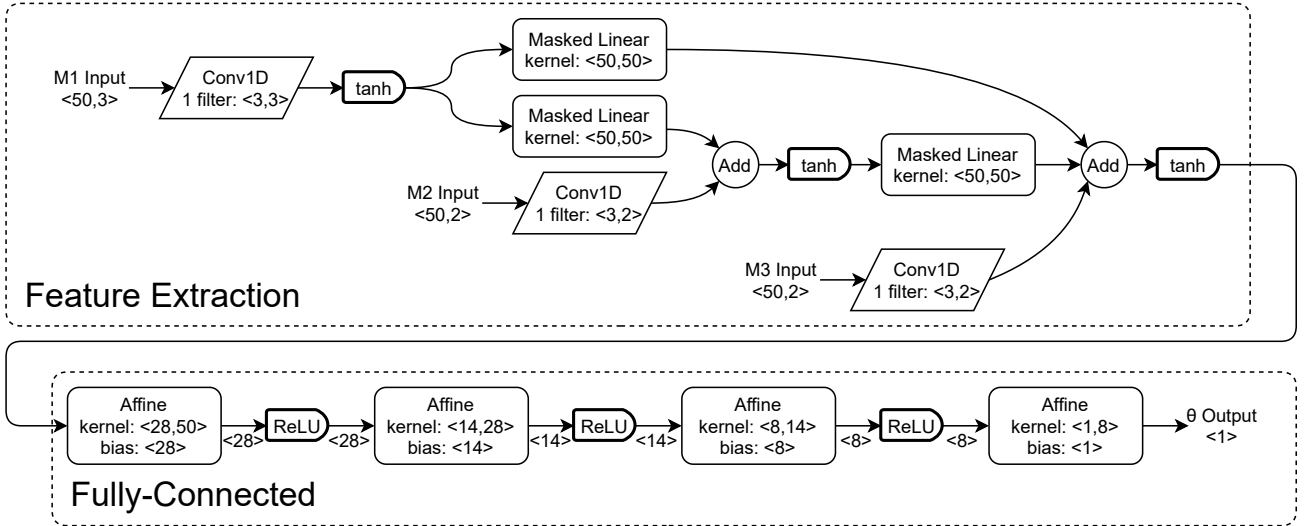


Figure 6: Schematic of the neural network optimized for the detector configuration. The kernel size for the **Affine** layers refers to (output dimension, input dimension). The kernel size for the **Conv1D** layers refers to filter size and (input channel, filter count). The <\*> notation on arrows indicates that the array shape passed through the arrow. Arrows without an array shape specified are passing arrays of shape 50.

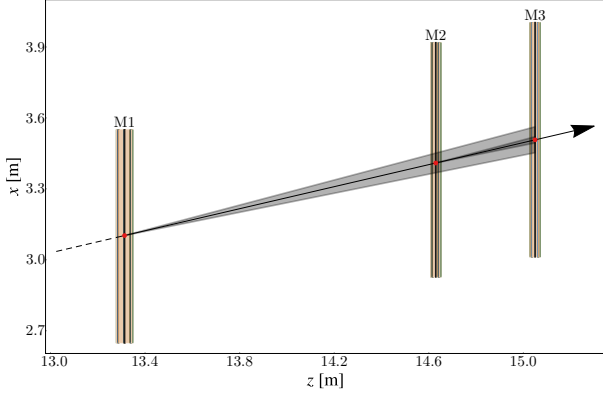


Figure 7: Demonstration of how the mask matrices work. The three black lines on the plates represent the observation and state vectors' position. The gray shaded cones represent the search region for a single hit on M1 or M2 marked red.

tization was applied to the trained **BL** network, further quantization-aware training was performed to mitigate the performance drop. These networks were quantized with 7, 5, and 3 float bits and are referred to as **QF7**, **QF5**, and **QF3**, respectively. All the networks were fully pipelined, like the networks described in Section 4, and were able to accept an event every 6.25 ns.

### 5.2. Performance

The angular resolution was evaluated from the widths of the distributions of the difference between the network output and the MC truth angle. Figure 8 shows the distributions for the **QF7** and **QF5** networks. The distribution of the ideal  $\chi^2$  method is also shown for reference. Table 2 shows the values of the angular resolution for the networks examined in this study. The angular resolution of the **QF7**, **QF5**, and **QF3** networks ranges from 2.0 to 2.8 mrad.

For the TGC detector at the ATLAS experiment at the HL-LHC, an average angular resolution of 4 mrad is assumed [8]. The angular resolution depends on the detector region, and the value obtained for  $2.13 < |\eta| < 2.16$ , which covers the  $\eta$  range of this study, is 2.4 mrad [26]. Although the detector configuration is not identical and thus the numbers cannot be compared directly, an angular resolution slightly greater than 2 mrad achieved by the **QF7** and **QF5** networks would be sufficient for the TGC detector.

The latency and the resource utilization were obtained for the quantized networks; the results are summarized in Table 2. Each quantized network was implemented on Vivado without timing violation and achieved a latency less than 100 ns. The resources were allocated by Vivado HLS on the basis of the number of bits involved in the calculations; some of multiplications performed by DSP48 in the **QF7** network are performed by LUTs in the **QF5** and **QF3** networks.

The **QF7** network was trained and evaluated on the datasets with artificial random noises. The model was

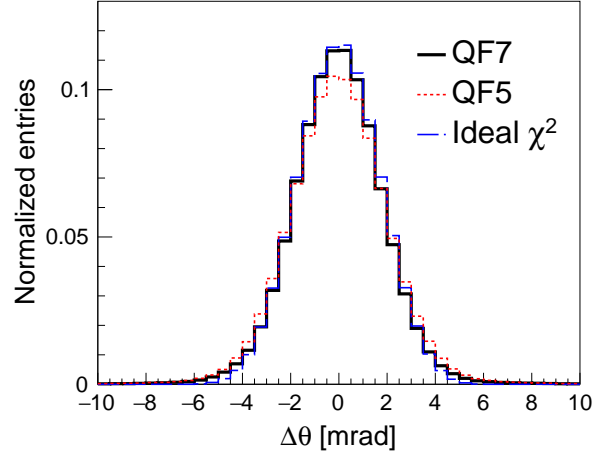


Figure 8: Distributions of the angle difference between the MC truth track segment and the reconstructed track segment. The solid (black) and dotted (red) histograms show the distributions for the track segments reconstructed by the **QF7** and **QF5** networks, respectively. The dashed (blue) histogram shows the distribution for track segments reconstructed by the ideal  $\chi^2$  method.

retrained on the noise levels of  $10^{-4}$  and  $10^{-3}$  and then implemented through Vivado. The angular resolution of the model at each noise level is shown in Table 3. With a reasonable noise level of  $10^{-4}$ , the network could still outperform the iterative  $\chi^2$  method; it maintained comparable performance at a noise level of  $10^{-3}$ .

## 6. Conclusion

Neural networks for fast tracking with multiwire proportional chambers were proposed and studied. A compact and quantized neural network was developed with a conventional CNN structure, where all the detector hits were inputted to a single convolution layer followed by multilayer perceptrons. A multistage neural network was then provided, where the outputs of the convolution layers for gas-gap groups were fed into multilayer perceptrons in sequence. The multistage neural network demonstrated better resource utilization and shorter latency for a given angular resolution of the tracking. The firmware was implemented in Xilinx UltraScale+ FPGA without timing violation and provided an angular resolution comparable with the best possible resolution of the detector estimated by the  $\chi^2$  method. A trigger turn-on curve similar to or better than that in Fig. 8.14 in Ref. [8], which was obtained using the  $\chi^2$  method, is expected with the neural networks developed in this study. The performance degraded moderately and was still acceptable with random noise hits. The firmware was able to perform one reconstruction in sub-100 ns with a fixed latency and have a high throughput of 160 MHz.

This work demonstrates a technique of forming a neural network and reducing the required resources for fast muon tracking using the hits of TGC-type detectors. Although

Table 2: The angular resolution, latency, and resource utilization for the neural networks optimized for the detector configuration of this study. The numbers in parentheses show the rates of resource utilization per super logic region. The angular resolution for **BL** is estimated using software, whereas those for **QF7**, **QF5**, and **QF3** are estimated using a Vivado post-implementation simulation. The **BL** network is provided without the intention to be run on the hardware; thus, the values of the latency and resource utilization are omitted.

Model	Resolution [mrad]	Latency [ns]	DSP48	LUT	FF	BRAM
<b>BL</b>	1.9	-	-	-	-	-
<b>QF7</b>	2.0	69	1389 (45%)	34,848 (8.1%)	5433 (0.6%)	75 (5.6%)
<b>QF5</b>	2.2	69	88 (2.9%)	40,039 (9.3%)	3419 (0.4%)	75 (5.6%)
<b>QF3</b>	2.8	56	2 (< 0.1%)	21,682 (5.0%)	2242 (0.3%)	75 (5.6%)

Table 3: Angular resolution in unit of milli-radians of the model trained on different datasets and implemented as **QF7**. The row headings are the noise level for the test sets, and the column headings are the noise level for the training sets.

Training \ Test	Test		
	0	$10^{-4}$	$10^{-3}$
0	2.0	2.2	3.3
$10^{-4}$	2.0	2.1	2.6
$10^{-3}$	2.1	2.1	2.3

the present networks will need further modifications and optimizations for a larger coverage of the detector and for a full trigger chain, the techniques shown in this paper can be exploited to maintain muon trigger thresholds in the HL-LHC era despite the greater luminosity.

## Acknowledgements

This work was supported by JSPS KAKENHI Grant Numbers 16H06493, 18K03675, and 21H05085.

## References

- [1] ATLAS Collaboration, Observation of a new particle in the search for the Standard Model Higgs boson with the ATLAS detector at the LHC, *Physics Letters B* 716 (1) (2012) 1–29. doi:<https://doi.org/10.1016/j.physletb.2012.08.020>.
- [2] CMS Collaboration, Observation of a new boson at a mass of 125 GeV with the CMS experiment at the LHC, *Physics Letters B* 716 (1) (2012) 30–61. doi:<https://doi.org/10.1016/j.physletb.2012.08.021>.
- [3] ATLAS Collaboration, Performance of the ATLAS muon trigger in pp collisions at  $\sqrt{s} = 8$  TeV, *The European Physical Journal C* 75 (2015) 120. doi:<https://doi.org/10.1140/epjc/s10052-015-3325-9>.
- [4] CMS Collaboration, The CMS trigger system, *Journal of Instrumentation* 12 (01) (2017) P01020. doi:<https://doi.org/10.1088/1748-0221/12/01/p01020>.
- [5] ATLAS Collaboration, A detailed map of Higgs boson interactions by the ATLAS experiment ten years after the discovery, *Nature* 607 (2022) 52–59. doi:<https://doi.org/10.1038/s41586-022-04893-w>.
- [6] CMS Collaboration, A portrait of the Higgs boson by the CMS experiment ten years after the discovery, *Nature* 607 (2022) 60–68. doi:<https://doi.org/10.1038/s41586-022-04892-x>.
- [7] I. B. Alonso, O. Brüning, P. Fessia, M. Lamont, L. Rossi, L. Tavian, M. Zerlauth, High-Luminosity Large Hadron Collider (HL-LHC): Technical design report (2020). doi:<https://doi.org/10.23731/CYRM-2020-0010>.
- [8] ATLAS Collaboration, Technical Design Report for the Phase-II Upgrade of the ATLAS TDAQ System (2018). URL <https://cds.cern.ch/record/2285584>
- [9] A Living Review of Machine Learning for Particle Physics. URL <https://iml-wg.github.io/HEPML-LivingReview/>
- [10] J. Duarte, S. Han, P. Harris, S. Jindariani, E. Kreinar, B. Kreis, J. Ngadiuba, M. Pierini, R. Rivera, N. Tran, Z. Wu, Fast inference of deep neural networks in FPGAs for particle physics, *Journal of Instrumentation* 13 (07) (2018) P07027. doi:<https://doi.org/10.1088/1748-0221/13/07/p07027>.
- [11] S. Summers, G. D. Guglielmo, J. Duarte, P. Harris, D. Hoang, S. Jindariani, E. Kreinar, V. Loncar, J. Ngadiuba, M. Pierini, D. Rankin, N. Tran, Z. Wu, Fast inference of Boosted Decision Trees in FPGAs for particle physics, *Journal of Instrumentation* 15 (05) (2020) P05026. doi:<https://doi.org/10.1088/1748-0221/15/05/p05026>.
- [12] J. Ngadiuba, V. Loncar, M. Pierini, S. Summers, G. D. Guglielmo, J. Duarte, P. Harris, D. Rankin, S. Jindariani, M. Liu, K. Pedro, N. Tran, E. Kreinar, S. Sagar, Z. Wu, D. Hoang, Compressing deep neural networks on FPGAs to binary and ternary precision with hls4ml, *Machine Learning: Science and Technology* 2 (1) (2020) 015001. doi:<https://doi.org/10.1088/2632-2153/aba042>.
- [13] C. N. Coelho Jr, A. Kuusela, S. Li, H. Zhuang, J. Ngadiuba, T. K. Aarrestad, V. Loncar, M. Pierini, A. A. Pol, S. Summers, Automatic heterogeneous quantization of deep neural networks for low-latency inference on the edge for particle detectors, *Nature Machine Intelligence* 3 (2021) 675–686. doi:<https://doi.org/10.1038/s42256-021-00356-5>.
- [14] CMS Collaboration, The Phase-2 Upgrade of the CMS Level-1 Trigger (2020). URL <https://cds.cern.ch/record/2714892>
- [15] ATLAS Collaboration, The ATLAS Fast TracKer system, *Journal of Instrumentation* 16 (07) (2021) P07006. doi:<https://doi.org/10.1088/1748-0221/16/07/P07006>.
- [16] W. Ashmanskas, A. Bardi, M. Bari, S. Belforte, J. Berryhill, M. Bogdan, A. Cerri, A. Clark, G. Chlachidze, R. Condorelli, R. Culbertson, M. Dell’Orso, S. Donati, H. Frisch, S. Galeotti, P. Giannetti, V. Glagolev, A. Leger, E. Meschi, F. Morzani, T. Nakaya, G. Punzi, L. Ristori, H. Sanders, A. Semenov, G. Signorelli, M. Shochet, T. Speer, F. Spinella, P. Wilson, X. Wu, A. Zanetti, Silicon vertex tracker: a fast precise tracking trigger for CDF, *Nuclear Instruments and Methods in Physics Research Section A: Accelerators, Spectrometers, Detectors and Associated Equipment* 447 (1) (2000) 218–222. doi:[https://doi.org/10.1016/S0168-9002\(00\)00190-X](https://doi.org/10.1016/S0168-9002(00)00190-X). URL <https://www.sciencedirect.com/science/article/pii/S016890020000190X>
- [17] M. Migliorini, J. Pazzini, A. Triossi, M. Zanetti, A. Zucchetta, Muon trigger with fast Neural Networks on FPGA, a demonstrator (2021). *arXiv:2105.04428[hep-ex]*. URL <https://arxiv.org/abs/2105.04428>
- [18] Xilinx, Vivado Design Suite. URL <https://www.xilinx.com>
- [19] S. Agostinelli, et al., Geant4—a simulation toolkit, *Nuclear Instruments and Methods in Physics Research Section A: Accelerators, Spectrometers, Detectors and Associated Equip-*



- ment 506 (3) (2003) 250–303. doi:[https://doi.org/10.1016/S0168-9002\(03\)01368-8](https://doi.org/10.1016/S0168-9002(03)01368-8).
- [20] ATLAS Collaboration, The ATLAS Experiment at the CERN Large Hadron Collider, *Journal of Instrumentation* 3 (08) (2008) S08003. doi:<https://doi.org/10.1088/1748-0221/3/08/s08003>.
- [21] F. Chollet, *et al.*, Keras (2015).  
URL <https://github.com/fchollet/keras>
- [22] M. Abadi, A. Agarwal, P. Barham, E. Brevdo, Z. Chen, C. Citro, G. S. Corrado, A. Davis, J. Dean, M. Devin, S. Ghemawat, I. Goodfellow, A. Harp, G. Irving, M. Isard, Y. Jia, R. Jozefowicz, L. Kaiser, M. Kudlur, J. Levenberg, D. Mané, R. Monga, S. Moore, D. Murray, C. Olah, M. Schuster, J. Shlens, B. Steiner, I. Sutskever, K. Talwar, P. Tucker, V. Vanhoucke, V. Vasudevan, F. Viégas, O. Vinyals, P. Warden, M. Wattenberg, M. Wicke, Y. Yu, X. Zheng, TensorFlow: Large-Scale Machine Learning on Heterogeneous Systems, software available from [tensorflow.org](https://www.tensorflow.org) (2015).  
URL <https://www.tensorflow.org/>
- [23] Xilinx, Vivado Design Suite User Guide: High-Level Synthesis (2021).  
URL [https://www.xilinx.com/support/documentation/sw\\_manuals/xilinx2020\\_1/ug902-vivado-high-level-synthesis.pdf](https://www.xilinx.com/support/documentation/sw_manuals/xilinx2020_1/ug902-vivado-high-level-synthesis.pdf)
- [24] K. Simonyan, A. Zisserman, Very deep convolutional networks for large-scale image recognition (2014). *arXiv:1409.1556[cs.CV]*.  
URL <https://arxiv.org/abs/1409.1556>
- [25] A. Hennequin, B. Couturier, V. Gligorov, S. Ponce, R. Quagliani, L. Lacassagne, A fast and efficient SIMD track reconstruction algorithm for the LHCb upgrade 1 VELO-PIX detector, *Journal of Instrumentation* 15 (06) (2020) P06018. doi:<https://doi.org/10.1088/1748-0221/15/06/p06018>.
- [26] ATLAS Collaboration, L0MuonTriggerPublicResults.  
URL <https://twiki.cern.ch/twiki/bin/view/AtlasPublic/L0MuonTriggerPublicResults>